

A numerical study of the F -model with domain-wall boundaries

Rick Keesman¹ and Jules Lamers^{2,3}

¹*Instituut-Lorentz, Universiteit Leiden, Niels Bohrweg 2, 2333 CA Leiden, The Netherlands*

²*Department of Mathematical Sciences, Chalmers University of Technology and University of Gothenburg, SE-412 96 Göteborg, Sweden*

³Corresponding author (julesl@chalmers.se)

We perform a numerical study of the F -model with domain-wall boundary conditions. Various exact results are known for this particular case of the six-vertex model, including closed expressions for the partition function for any system size as well as its asymptotics and leading finite-size corrections. To complement this picture we use a full lattice multi-cluster algorithm to study equilibrium properties of this model for systems of moderate size, up to $L = 512$. We compare the energy to its exactly known large- L asymptotics. We investigate the model's infinite-order phase transition, by means of finite-size scaling for an observable derived from the staggered polarization, to test the method put forward in our recent joint work with Duine and Barkema. In addition we analyse local properties of the model. Our data are perfectly consistent with analytical expressions for the arctic curves. We investigate the structure inside the temperate region of the lattice, confirming the oscillations in vertex densities recently observed by Lyberg et al., which appear to be finite-size effects. We point out different types of oscillations, notably including '(anti)ferroelectric' oscillations close to the corresponding frozen regions, as well as 'higher' oscillations forming an intricate pattern with 'saddle-point'-like features.

I. INTRODUCTION

The F -model for antiferroelectric materials [2] is a special case of the six-vertex, or ice-type, model that exhibits an infinite-order phase transition (IOPT) [3]. Amongst others, studying the F -model may thus be instructive to get a better grasp of the well-known IOPT of the two-dimensional XY -model as it offers a more simple setting in which the microscopic degrees of freedom are discrete. By definition, at an IOPT the physics of a system does not change as abruptly as it does for finite-order phase transitions, which makes numerical investigations a rather subtle issue. In [4], together with Duine and Barkema, we proposed a new observable for numerical studies of IOPTs: the logarithmic derivative of the (smooth but not analytic) order parameter for the IOPT. By construction this quantity exhibits a peak at the critical — or rather 'transition' — temperature β_c of the model, which makes it a suitable candidate for the analysis of the physics near the IOPT. We used a finite-size scaling analysis to compare the performance of our observable with that of other observables commonly used in the literature, focussing on the F -model with periodic boundary conditions (PBCs) in both directions. In the present work we test the observable in a different, yet closely related, setting. At the same time this allows us to investigate other intriguing features of the F -model, such as the dependence of its thermodynamics, i.e. the behaviour at asymptotically large system size, on the boundary conditions.

The microscopic degrees of freedom of the six-vertex model are arrows pointing in either direction along the edges of a square lattice. Around each vertex the arrows have to obey the so-called ice rule, which turns out to be rather restrictive [1]. On the one hand this condition famously allows for a Bethe-ansatz analysis that

provides *exact* results, see e.g. [6] and references therein, in the thermodynamic limit. On the other hand it causes the model's thermodynamics to depend on the *choice of boundary conditions* used at the intermediate analysis for finite size [7, 8]. (In fact, this phenomenon in the context of graphene [9] originally motivated [4] and the present work.) PBCs are commonly employed and are compatible with the translational invariance that is present for infinite systems. For the six-vertex model this choice is important for the Bethe ansatz, cf. [3]. This choice was also used in our previous work [4]. The same thermodynamic behaviour is obtained for 'free' and 'Néel' boundary conditions, where the arrows on the external edges are respectively left free or fixed to alternate [10, 11]. This is not true for 'ferroelectric' boundary conditions, where the arrows at the boundary all point e.g. up or to the right, but with a single allowed microstate the resulting thermodynamics is trivial.

An interesting intermediate case is provided by *domain-wall boundary conditions* (DWBCs), where on two opposite boundaries the arrows all point outwards whereas on the other two boundaries all arrows point inwards. Such boundary conditions first appeared in the calculation of norms of Bethe vectors in the quantum inverse-scattering method (QISM) in the work of Korepin [12]. Indeed, the QISM allows for an algebraic construction of the Bethe-ansatz vectors for the Heisenberg XXX and XXZ spin chains and the six-vertex model with PBCs. These algebraic Bethe-ansatz vectors simultaneously diagonalize the spin-chain Hamiltonian and the transfer matrix of the six-vertex models provided the parameters featuring in the ansatz obey constraints known as the Bethe-ansatz equations, see e.g. [6]. The partition function of the six-vertex model with DWBCs, also known as the *domain-wall partition function*, is related to the norm of the algebraic Bethe-ansatz vec-

tors [12]. Later this quantity was found to have applications ranging from the combinatorics of alternating-sign matrices [13, 14] (see also the book [15]) to three-point amplitudes in $\mathcal{N} = 4$ super Yang-Mills theory [16].

The domain-wall partition function admits a concise closed expression for all system sizes [16]. From this the infinite-size asymptotics can be found [7, 17], as well as the form of the leading finite-size corrections [18–20]. The phase diagram of the six-vertex model has the same form for PBCs and DWBCs, but the details are different [7, 17, 21]; for example, even though the F -model exhibits an IOPT in both cases, the free energy per site of the F -model is larger for DWBCs than for PBCs. In the past decade or so DWBCs have also attracted considerable attention in relation to the arctic-curve phenomenon: they lead to coexisting phases that are spatially separated, with an *arctic curve* separating the ‘frozen’ (ordered) and ‘temperate’ spatial regions. This has been investigated from numerical [22–24] as well as analytic [25–29] viewpoints.

The remainder of this paper is organized as follows. In Sec. II we review the F -model with DWBCs, its partition function, and the relevant observables; in particular we give a description of the staggered six-vertex model in the framework of the QISM based on [30]. The Monte Carlo cluster algorithm and data processing are discussed in Sec. III. The results are treated in Sec. IV. We fit the exact asymptotic expressions for the energy, giving best estimates for the free parameters in the finite-size corrections, and perform a finite-size scaling analysis to test our observable at the IOPT. Besides these average properties we use our simulations to examine local properties: the coexisting phases, arctic curves, and the structure in the temperate region of the lattice. We conclude with a summary and outlook in Sec. V.

II. THEORY

A. The F -model and domain walls

The six-vertex model, or (energetic) ice-type model, is a vertex model on a square lattice. The arrows on the edges are restricted by the *ice rule*, which demands that at every vertex two arrows point inwards and two point outwards. This leaves for the six allowed vertex configurations shown in Fig. 1. To each vertex configuration i one assigns (local) Boltzmann weight $\exp(-\beta \epsilon_i)$, with $\beta := 1/(k_B T)$ the inverse temperature, k_B the Boltzmann constant that we put to unity from here on, and ϵ_i the energy of the vertex configuration. The energy is additive, so the weight of a configuration is the product of these local weights. Summing these over all allowed configurations, subject to some boundary conditions, one obtains the model’s partition function.

The F -model can be obtained by taking $\epsilon_1 = \epsilon_2 = \epsilon_3 = \epsilon_4 = \epsilon > 0$ and $\epsilon_5 = \epsilon_6 = 0$, with corresponding vertex weights related by $a = b = \exp(-\beta \epsilon) c$, making vertices

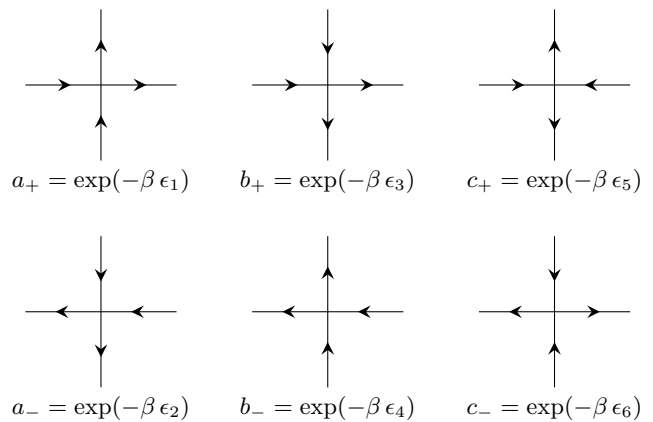


Figure 1. The six vertices allowed by the ice rule and their weights for six-vertex model. Often one assumes global arrow-reversal symmetry: $a_{\pm} = a$, $b_{\pm} = b$, $c_{\pm} = c$. The F -model is defined by $a = b < c$.

5 and 6 energetically favourable. The phase diagram is shown in Fig. 2. For low enough temperatures the system is in the antiferroelectric phase (AF). As temperature increases there is a transition to the disordered phase (D). For PBCs the ground state consists of vertices 5 and 6 alternating in a checkerboard-like manner; this global AF order persists throughout region (AF) and is destroyed upon entering (D).

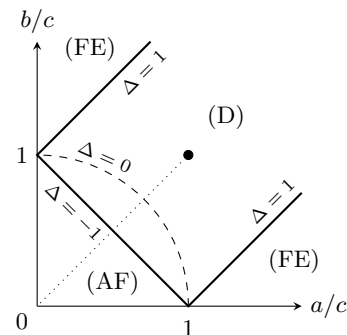


Figure 2. The phase diagram of the six-vertex model, parametrized by the ratios a/c and b/c since simultaneous rescalings of the vertex weights only yield an overall factor for the partition function. The dashed arc is the so-called free-fermion line. The dotted line corresponds to the F -model, with an infinite-order phase transition between the antiferroelectric (AF) and disordered (D) phase. The thick dot is the ice point $a = b = c$, which can be interpreted as $\beta = 0$.

The six-vertex model does not have a thermodynamic limit in the usual sense: the physical properties of macroscopic systems remain sensitive to the choice of boundary conditions. Rather than imposing PBCs we consider an $L \times L$ portion of the lattice with *domain-wall boundary conditions* (DWBCs), where the arrows on external edges are fixed and point out (inwards) on all horizontal (vertical) edges, say. This change in boundary conditions

has several interesting consequences that will be reviewed momentarily. Similarly to the case of PBCs one obtains exact results for the DWBC F -model by extending it to the six-vertex model with general vertex weights a , b , and c as in Fig. 1. The ‘reduced coupling constant’ is defined as

$$\Delta := \frac{a^2 + b^2 - c^2}{2ab}. \quad (1)$$

The phase diagram looks again like in Fig. 2. At high temperatures the system is in the disordered phase (D), $-1 < \Delta < 1$. As the temperature is lowered it transitions into the antiferroelectric phase (AF), $\Delta < -1$, or one of the two ferroelectric phases (FE), $\Delta > 1$, depending on the ratio $a : b : c$. The phase transition between (D) and (AF) is of infinite order for PBCs [3] as well as DWBCs (cf. the end of the following subsection) [17, 20], while those between (D) and (FE) are of first order for PBCs [31] but of second order for DWBCs [7, 32].

In (FE) the DWBCs are compatible with the FE order, while for $\Delta < 1$ (including the F -model) the boundaries raise the free energy per site with respect to the case of PBCs. Zinn-Justin [8] suggested that this can be understood as a consequence of coexisting phases that are spatially separated. This phenomenon had also been found for various choices of fixed boundary conditions for the ice model ($a = b = c$) before [33]. Through the ice rule the DWBCs induce ordered regions that extend deep into the bulk, and translational invariance is lost even far away from the boundary. For example, the ground state is no longer a checkerboard-like configuration of vertices 5 and 6 as for PBCs, which would after all lead to alternating arrows along the boundary. Instead the DWBC ground state consists of a central diamond-shaped area with AF order (see also Fig. 7 (a) below), consisting of vertices 5 and 6 like before, enclosed by corners that each possess FE order, containing a homogeneous configuration of one of the vertices 1 to 4. (When L is even there are two ground-state configurations of this form.) The domain walls thus raise the ground-state energy per site in the thermodynamic limit from 0 for PBCs to $\epsilon/2$ for DWBCs. When the temperature becomes nonzero a disordered region appears that separates the regions of AF and FE order, and above the critical temperature the region with AF order disappears to leave a central disordered region surrounded by FE ordered regions [22, 23]. There are sharp transitions between the regions, and the curves separating the ‘frozen’ (AF or FE ordered) and ‘temperate’ regions in the scaling limit (i.e. let $L \rightarrow \infty$ while decreasing the lattice spacing to keep total system size fixed) are known as *arctic curves*. These curves have four contact points with the boundary, which for the F -model lie in the middle of each side [28]. For the ‘free-fermion point’ $\Delta = 0$ the arctic curve is a circle [25] up to fluctuations of order $\sim L^{1/3}$ governed by an Airy process [26]. The arctic curve has also been conjectured for $|\Delta| < 1$ [27, 28] and $\Delta < -1$ [29], where the latter focusses on the curve separating the FE and D regions.

Because we are interested in the F -model from now on we focus on (D) and (AF). The following (real) parametrization of the vertex weights are often used in these regimes:

$$(D): \begin{cases} a = \sin(\gamma - t) \\ b = \sin(\gamma + t) \\ c = \sin 2\gamma \end{cases}, \quad (AF): \begin{cases} a = \sinh(\gamma - t) \\ b = \sinh(\gamma + t) \\ c = \sinh 2\gamma \end{cases}. \quad (2)$$

Here $t \in [-\gamma, \gamma]$ is called the spectral parameter, while $\gamma \geq 0$ is the crossing parameter, which for (D) is further restricted to $\gamma < \pi/2$; it is related to (1) via $\Delta = -\cos 2\gamma$ for (D) and $\Delta = -\cosh 2\gamma$ for (AF). The F -model then corresponds to $t = 0$, with $\Delta = 1 - e^{2\beta\epsilon}/2$ or γ encoding the temperature as

$$e^{\beta\epsilon} = \frac{c}{a} = \frac{c}{b} = \begin{cases} 2 \cos \gamma, & \gamma \in [0, \pi/3] \quad (D), \\ 2 \cosh \gamma, & \gamma \geq 0 \quad (AF). \end{cases} \quad (3)$$

The phase transition of the F -model occurs at $\beta_c \epsilon = \ln 2$ ($\Delta = -1$, $\gamma = 0$). At this point the parametrization (2) vanishes identically, which can be avoided by simultaneously rescaling the weights to set c equal to unity. At the level of the partition function this may be implemented by keeping (2) with $t = 0$ but considering the ‘renormalized’ partition function $c^{-L^2} Z_L(a, b, c) = Z_L(a/c, b/c, 1)$. We will denote this quantity simply by Z_L .

B. The domain-wall partition function

In some sense the six-vertex model with DWBCs is a theorist’s dream. Unlike for PBCs, for which exact results are only available for asymptotically large systems, the domain-wall partition function Z_L can be found exactly for *all* system sizes. In brief the computation goes as follows, see e.g. [14] for more details. For the i th row (j th column) of the lattice one introduces a parameter u_i (v_j). This allows one to further extend the model to an inhomogeneous version where the weight (2) at position (i, j) features $u_i - v_j$ instead of t . Korepin [12] showed that Z_L , viewed as a function of the u_i , obeys certain properties that determine it uniquely in the inhomogeneous setting; most importantly there is a recursion relation that expresses Z_L with one u_i specialized to a specific value in terms of Z_{L-1} . Izergin [16, 34] found a remarkably concise expression in the form of a determinant of an $L \times L$ matrix. Since it meets all Korepin’s requirements, Izergin’s determinant provides a formula for the domain-wall partition function valid for all L . Upon carefully evaluating the homogeneous limit, $u_i - v_j \rightarrow t$ for all i and j , this results in a Hankel determinant:

$$Z_L = \frac{(ab/c)^{L^2}}{\prod_{k=0}^{L-1} (k!)^2} \det_{L \times L} M, \quad M_{i,j} := \partial_t^{i+j-2} \frac{c}{ab}, \quad (4)$$

where the definition of $M_{i,j}$ assumes a parametrization of the form (2). Specializing this quantity to the ice (or

‘combinatorial’) point $a = b = c$ (so $\Delta = 1/2$) one finds that the number of domain-wall configurations for $L = 1, 2, \dots$ is $1, 2, 7, 42, 429, 7436, 218348, \dots$ [14]. For the F -model the domain-wall partition function factorizes as $Z_{2L} = 2 X_{2L} X_{2L+1}$, $Z_{2L+1} = X_{2L+1} X_{2L+2}$ for certain polynomials X_L [14, Thm. 3], cf. [35, Thm. 4].

Using the explicit results found by Korepin–Izergin the bulk free energy was evaluated in the thermodynamic limit by Korepin and Zinn-Justin [7] and Zinn-Justin [17]. Prior to that only some special cases in (D) were known: the free-fermion point ($\Delta = 0$, $\gamma = \pi/4$) corresponding to the 2-enumeration of alternating-sign matrices [13, Sec. 6], and the ice point ($\Delta = 1/2$, $\gamma = \pi/3$) as well as the point $\Delta = -1/2$ ($\gamma = \pi/6$) related to the 3-enumeration of alternating-sign matrices [14]. Here we recall that the ‘ c^2 -enumeration of alternating-sign matrices’, cf. e.g. [14, 15], is given by $c^L Z_L(1, 1, c)$ since the DWBCs imply that $\# c_- = L + \# c_+$.

A rigorous and more detailed analysis for (D), (AF) and the corresponding phase transition, which is most relevant for us, was given by Bleher et al. [18–20]. The asymptotic expressions for the domain-wall partition function Z_L , together with the first subleading terms in system size, are as follows for the F -model. In the disordered regime one has [18]

$$Z_D^{\text{asym}} = C_D(\gamma) f_D(\gamma) L^{\kappa(\gamma)} [1 + O(L^{-\alpha})], \quad (5)$$

where $C_D(\gamma) > 0$ and $\alpha > 0$ are unknown, while

$$f_D(\gamma) = \frac{\pi \tan \gamma}{4\gamma}, \quad \kappa(\gamma) = \frac{1}{12} - \frac{2\gamma^2}{3\pi(\pi - 2\gamma)}. \quad (6)$$

For the antiferroelectric regime one finds [19]

$$Z_{\text{AF}}^{\text{asym}} = C_{\text{AF}}(\gamma) f_{\text{AF}}(\gamma) L^2 \vartheta_4(L\pi/2) [1 + O(L^{-1})], \quad (7)$$

with $C_{\text{AF}}(\gamma) > 0$ another unknown normalization factor, and the extensive part of the free energy is

$$f_{\text{AF}}(\gamma) = \frac{\pi \tanh \gamma}{4\gamma} \frac{\vartheta'_1(0)}{\vartheta_1(\pi/2)}, \quad (8)$$

where ϑ_1 and ϑ_4 denote the Jacobi theta functions with temperature-dependent elliptic nome $q := \exp(-\pi^2/2\gamma)$.

From these exact asymptotics of the domain-wall partition function it can be shown that the phase transition is of infinite order [17, 20]. Indeed, when subtracting the regular part, $(\pi/4\gamma) \tanh \gamma$ [differing from (6) only in the parametrization used], from the AF free energy (8) one is left with an expression that is smooth but exhibits an essential singularity as $\gamma \rightarrow 0^+$.

C. The staggered polarization

An order parameter for the (D)–(AF) phase transition is defined as follows. For any microstate C one can compute the spontaneous staggered polarization $P_0(C)$.

This quantity is a measure of the likeness of C to one of the two AF ground states C' of the system with PBCs. At each vertex the local spontaneous staggered polarization can be defined as $\sum_i \sigma_i \sigma'_i / 4$, where the sum is taken over the four edges surrounding the vertex, and $\sigma_i = \pm 1$ ($\sigma'_i = \pm 1$) depending on whether arrows on those edges point outwards or inwards in C (C'). Then $P_0(C)$ is the sum over all these local quantities; since the AF ground state is two-fold degenerate its sign depends on the choice of C' to which C is compared. Additionally, for even L states come in pairs with equal energy but opposite spontaneous staggered polarization. To avoid cancellation of these contributions one defines the *staggered polarization* as the thermal average $P_0 := \langle |P_0(C)| \rangle$ of the absolute value of $P_0(C)$. Note that the situation is analogous to what happens for the magnetization in the two-dimensional Ising model.

For the system with PBCs Baxter derived the exact large- L asymptotics of P_0 for all temperatures [30]. This quantity becomes smoothly nonzero when the system transitions from (D) to (AF). Let us assume that it continues to be a valid order parameter for the transition of the system with DWBCs. For this case an expression for P_0 that is manageable for all system sizes is not known. We still have

$$P_0 = \left. \frac{d \ln Z_L^+(s)}{ds} \right|_{s=0}, \quad (9)$$

where $Z_L(s)$ is the partition function of the F -model on an $L \times L$ lattice with DWBCs in the presence of an external staggered electric field of strength $s \geq 0$. The superscript ‘+’ in (9) indicates that the absolute value of each coefficient is to be taken in order to prevent the aforementioned cancellation. No analogue of (4) is known when $s \neq 0$. Nevertheless the framework of the quantum inverse-scattering method (QISM) does allow for the direct computation of $Z_L(s)$, and thus P_0 , for low system size. Let us indicate how this works; we refer to [6] and references therein for more about the QISM.

Let us give a description of the *staggered six-vertex model* based on Baxter [30]. We focus on the homogeneous case; inhomogeneities may be incorporated as usual. View the square lattice as being bipartite by dividing its vertices into two sets in a checkerboard-like manner. The vertex weights from Fig. 1 are given by $a_{\pm} = a$, $b_{\pm} = b$, while c_{\pm} is equal to $e^{\pm s} c$ on one sublattice (‘black’ vertices) and to $e^{\mp s} c$ on the other (‘white’ vertices). These vertex weights can be encoded in the so-called R -matrix [5]

$$R(s) = \begin{array}{c} \text{---} \bigcirc \text{---} \\ \text{---} \end{array} = \begin{pmatrix} a & 0 & 0 & 0 \\ 0 & b & e^s c & 0 \\ 0 & e^{-s} c & b & 0 \\ 0 & 0 & 0 & a \end{pmatrix}, \quad (10)$$

defined with respect to the basis $|\nearrow, \nearrow\rangle, |\nearrow, \searrow\rangle, |\nwarrow, \nwarrow\rangle, |\nwarrow, \searrow\rangle$ for the ‘incoming’ lines and $\langle \nearrow, \nearrow|, \langle \searrow, \searrow|, \langle \nwarrow, \nwarrow|, \langle \nwarrow, \searrow|$ for the ‘outgoing’ lines at the vertex. In the diagrammatic

notation in (10) one should think of time running along the diagonal from bottom left to top right. $R(s)$ contains the vertex weights for the ‘black’ vertices and $R(-s)$ for the ‘white’ vertices.

A row of the lattice is described by the staggered (row-to-row) *monodromy matrix*

$$T(s) := \begin{array}{c} \text{---} \bigcirc \text{---} \bigcirc \text{---} \cdots \text{---} \bigcirc \text{---} \\ \text{---} \text{---} \text{---} \text{---} \text{---} \text{---} \text{---} \text{---} \text{---} \\ \text{---} \text{---} \text{---} \text{---} \text{---} \text{---} \text{---} \text{---} \end{array} \quad (11)$$

1 2 L

$$= R_L(\pm s) \cdots R_2(-s) R_1(s),$$

where R_j contains the weights for the j th vertex in that row. It is customary to write $B(s)$ for the $2^L \times 2^L$ matrix sitting in the upper right quadrant of $T(s)$. This matrix accounts for a row of the staggered six-vertex model with arrows on the horizontal external edges pointing outwards as for DWBCs:

$$B(s) = \begin{array}{c} \leftarrow \bigcirc \text{---} \bigcirc \text{---} \cdots \text{---} \bigcirc \rightarrow \\ \text{---} \text{---} \text{---} \text{---} \text{---} \text{---} \text{---} \text{---} \end{array} \quad (12)$$

1 2 L

The staggered domain-wall partition function can then be expressed as an entry of a ‘staggered’ product of L such matrices [36]:

$$Z_L(s) = \langle \downarrow \downarrow \cdots \downarrow | B(\pm s) \cdots B(-s) B(s) | \uparrow \uparrow \cdots \uparrow \rangle. \quad (13)$$

For example, if $L = 1$ then $B(s)$ is $\begin{pmatrix} 0 & 0 \\ e^s & c \end{pmatrix}$ and $Z_1(s) = e^s c$. The ordinary domain-wall partition is recovered in this algebraic language as $Z_L = Z_L(0)$. We have evaluated (13) for general s up to $L = 12$, accounting for little over 10^{16} configurations.

To conclude this section let us comment on whether quantum integrability may be used to get some concise expression for $Z(s)$ valid for all L . The answer appears to be negative; at least the Korepin–Izergin approach mentioned in Sec. II B does not simply extend to $s > 0$. Indeed, one can still write down four recursion relations obeyed by the inhomogeneous extension of (13), namely for $u_1 = v_1 - \gamma$, $u_1 = v_L + \gamma$, $u_L = v_1 + \gamma$ and $u_L = v_L - \gamma$. However, for $s \neq 0$ the inhomogeneous partition function is not symmetric in the u_i , so one does not get further Korepin-like recursion relations and the conditions do not uniquely determine $Z(s)$ for general L . The failure of $Z(s)$ to be symmetric in the u_i is of course closely related to the fact that the staggered R -matrices (10) do not obey a Yang–Baxter equation — even writing down the latter is problematic since the triangle featuring in that relation is not bipartite.

III. SIMULATIONS

Recall that the six-vertex model is equivalent to a height model known as the (body-centred) solid-on-solid

model [38]. In this picture fixed boundary conditions ensure that the height of a configuration is bounded from below and above. Going around the boundary in some direction the DWBCs correspond to the height increasing along two opposite ends, say from 0 to L , and then decreasing from L back to 0 along the other two ends. There are unique configurations of minimal and maximal height: the former corresponds to a valley of height 0 running along one diagonal, and the latter to a ridge of height L along the other diagonal. (The ground state corresponds to a diamond-shaped plateau, of height as close as possible to $L/2$, surrounded by steep slopes to the pits and peaks at the corners.) The existence of configurations of minimal and maximal height allows one to use *coupling from the past* (CFTP) algorithms [39], which ensure that one draws configurations from the equilibrium distribution making it a perfect simulation. Although CFTP can in principle be ‘shelled’ around a variety of updating schemes, in practice it is only used in combination with local updates due to the difficulties that arise when the same global update needs to be performed on both the lower and higher configuration. In this work we prefer speed over sample accuracy as this allows us to investigate much larger systems, thus improving the reliability of our subsequent analysis of the thermodynamic limit. Rather than CFTP we thus use the full lattice multi-cluster algorithm [40], as in [4], with a reported dynamic exponent $z = 0.005 \pm 0.022$ for PBCs [41], so that the correlation time can be considered independent of system size in practice. The accuracy of our simulations is checked in Sec. IV against the theoretical expressions that were reviewed in Sec. II.

Our results are procured from Monte Carlo simulations using the full lattice multi-cluster algorithm in combination with parallel tempering [42]. We use the multi-histogram method [43, 44] to interpolate observables in a temperature range around the critical temperature. The F -model is well suited for both parallel tempering and the multi-histogram method as the specific heat is analytically known and bounded, cf. (14) below, such that a set of temperatures can be constructed a priori at which the energy distributions of ‘adjacent’ configurations overlap significantly. Given a configuration at inverse temperature β , its neighbouring configurations are set at $\beta' = \beta \pm \beta/\sqrt{C_v}$. In each simulation the acceptance probability of swapping two configurations is never less than 47%. After each update a measurement is taken, with a minimum of 10^6 measurements per system size per temperature, at up to 30 different temperatures per system size. Note that all cluster updates that would change the arrows on the boundary are rejected to preserve the DWBCs.

IV. RESULTS

A. Energy and specific heat

Unlike the energy, the partition function itself can not be directly measured in Monte Carlo simulations. Exceptions are very small systems ($L \leq 6$) for which our simulations happen to sample all microstates so that we are able to reconstruct the full staggered partition function. The resulting expressions for $E(\beta) = \langle E(C) \rangle$ and $P_0(\beta)$ precisely match those obtained via the QISM as described in Sec. II C. In general just a part of the phase space is sampled so the partition function cannot be reconstructed as the total energy $E(\beta)$ is not known for all temperatures. However, the multi-histogram method allows us to use simulations done at finitely many temperatures to determine the partition function, up to an overall factor, on some finite temperature range.

Fig. 3 shows the energy per site $e(\beta) := E(\beta)/L^2$ and the specific heat per site $c_v(\beta) := C_v(\beta)/L^2$ as functions of inverse temperature. The simulation data is shown together with the exact expressions for infinite size extracted from Eqs. (5) and (7) using

$$E(\beta) = -\frac{\partial \ln Z}{\partial \beta}, \quad \frac{C_v(\beta)}{\beta^2} = -\frac{\partial E}{\partial \beta} = \frac{\partial^2 \ln Z}{\partial \beta^2}, \quad (14)$$

which yields $e(\beta_c) = 2/3$ and $c_v(\beta_c) = 8 \ln^2(2)/45$. We observe a convergence of the simulation data to the analytically known asymptotic values over all simulated temperature ranges.

To investigate the effects of the subleading corrections in the system size for the partition function further we focus on the critical point. Because of the smoothness of the partition function we can take the expressions for the disordered regime and evaluate them at the phase transition. Starting from Eq. (5) we find the following expression for the energy per site $e_L(\beta_c)$ at the critical point for system size L :

$$e_L(\beta_c) = \frac{2}{3} - \frac{4}{3\pi^2} \frac{\ln L}{L^2} - \frac{C_1}{L^2} + O(L^{-(\alpha+2)}), \quad (15)$$

with $C_1 = -\lim_{\gamma \rightarrow 0+} C'_D(\gamma)/[\gamma C_D(\gamma)]$ an unknown parameter. Eq. (15) can be checked against the expression for the energy derived directly from (4) for small system sizes ($L \leq 16$) as well as the simulation data for moderate system sizes. This is shown in Fig. 4 where $e_\infty(\beta_c) - e_L(\beta_c)$ and $E_\infty(\beta_c) - E_L(\beta_c)$ are plotted versus system size. The best unweighed fit, including only the asymptotically next-to-leading correction $C_1 = 0.669 \pm 0.019$, already shows very good agreement with both the exact and numerically obtained values. For $L \leq 141$ this next-to-leading correction, $\sim 1/L^2$, is more important than the asymptotically leading correction, $\sim \ln L/L^2$. This means that even at $L \sim 10^{21}$ the two corrections in (15) just differ by a factor 10. Also note the high precision at which both the leading and first subleading corrections

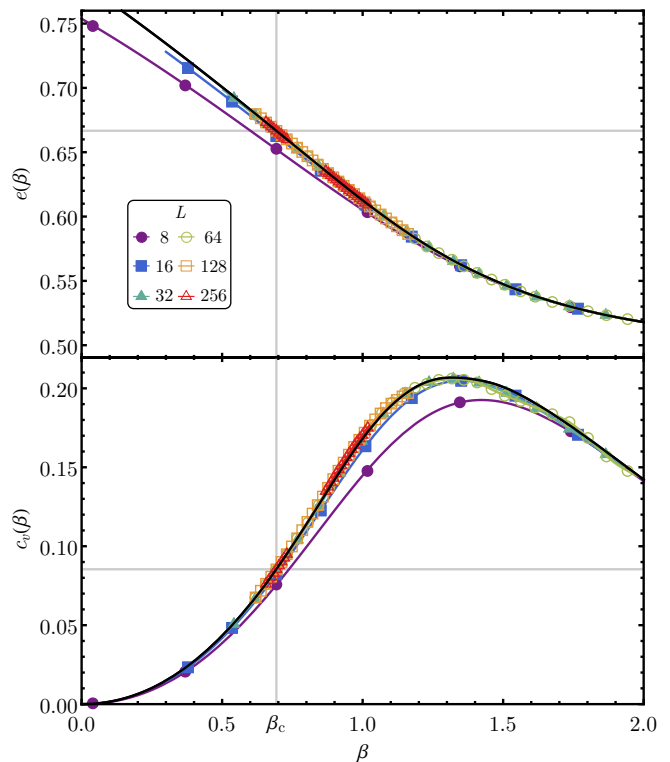


Figure 3. The average energy per site $e(\beta)$ (top) and specific heat per site $c_v(\beta)$ (bottom) as functions of inverse temperature β . The critical points at β_c are indicated by the gray lines. The black lines are the exact asymptotic expressions extracted from Eqs. (5) and (7). From the data points, indicating the temperatures at which the simulations are done, the coloured solid lines are calculated using the multi-histogram method. For both observables we see a convergence of the data to the analytically known expressions in the thermodynamic limit.

are measurable for systems as large as $L = 256$, for which these corrections are of the order 10^{-5} .

A best estimate for the value of α can be found by assuming that the subleading terms in (5), i.e. the $O(L^{-\alpha})$, is of the form $g(\gamma) L^{-\alpha}$. This yields

$$e_L(\beta_c) \simeq \frac{2}{3} - \frac{4}{3\pi^2} \frac{\ln L}{L^2} - \frac{C_1}{L^2} + \frac{C_2}{L^2(L^\alpha + C_3)}, \quad (16)$$

where $C_2 = \lim_{\gamma \rightarrow 0+} g'(\gamma)/\gamma$ and $C_3 = \lim_{\gamma \rightarrow 0+} g(\gamma)$ are again unknown. We assume that these limits make sense; the corrections are finite and must disappear for infinite systems. If we use our best value for C_1 and fit Eq. (16) to the energies of small systems obtained from direct computation of (13), see again Fig. 4, the best estimates are $C_2 = 1.6 \pm 1.2$, $C_3 = 14 \pm 12$ and $\alpha = 1.91 \pm 0.36$. The inclusion of these subleading correction does improve the fit qualitatively although error margins for best estimates of the parameters C_2 and C_3 are very large. With these values the crossover point where the terms proportional to C_1 and C_2 become comparable occurs already at $L = 3.9$. The exact analytical values for the energy

can be computed using (4) or (13). We have done so for $L \leq 16$; in either case most computation time was spent on the derivation of the energy from the partition function at the critical point rather than the calculation of the partition function itself.

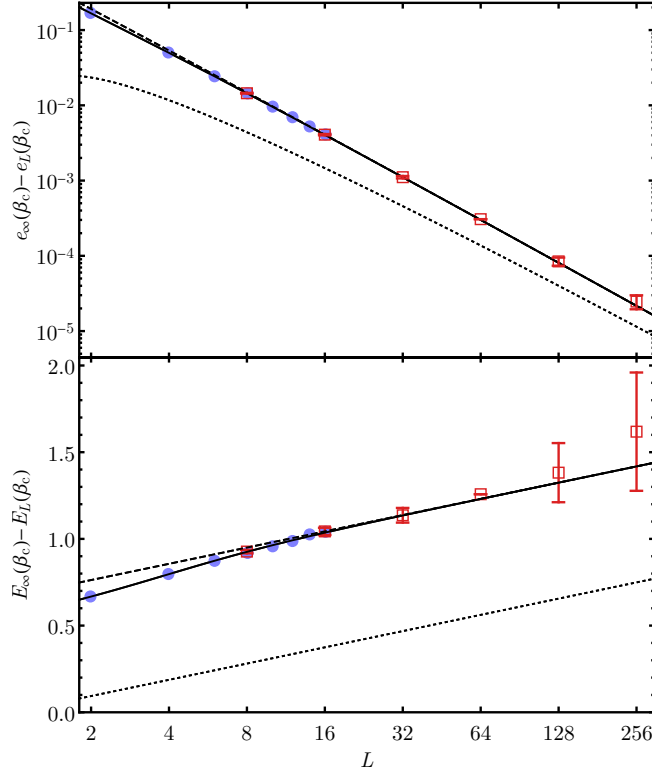


Figure 4. The difference between the energy per site (top) and total energy of the system (bottom), with $E_\infty(\beta_c) := L^2 e_\infty(\beta_c) = 2L^2/3$, is shown as a function of system size. The solid blue disks represent the exact known values for small system sizes obtained from Eq. (4). The open red squares denote best estimates obtained from our simulations. The error bars are estimates based on the fluctuations in the energy and the number of measurements taken. The expressions from Eq. (15) with only the leading correction ($C_1 \equiv C_2 \equiv 0$) and with first subleading correction ($C_1 = 0.669 \pm 0.018$), as well as the expression from Eq. (16) ($\alpha = 1.91 \pm 0.36$, $C_2 = 1.6 \pm 1.2$, $C_3 = 14 \pm 12$) are shown as black dotted, dashed, and solid lines, respectively.

B. The logarithmic derivative of P_0

Similar to our work in [4] we now study $d \ln P_0 / d\beta$, which must have a peak at the critical point for infinitely large systems if P_0 is a true observable of the infinite-order phase transition. As for the energy the multi-histogram method is used to obtain $d \ln P_0 / d\beta$ by interpolation between the temperatures at which the systems were simulated. Fig. 5 (a) shows $d \ln P_0 / d\beta$ as a function of inverse temperature for various system sizes

up to linear size $L = 256$. To obtain a numerical collapse for each system size we determine the peak coordinates (β_{\max}, h_{\max}) as well as the typical width w , which is defined as the absolute difference between β_{\max} and the lower temperature at which $d \ln P_0 / d\beta$ attains 95% of the peak height. The numerical collapse is shown in Fig. 5 (b); unfortunately it is less clean than its counterpart for PBCs in [4].

Previously we found behavioural similarities between $d \ln P_0 / d\beta$ and the susceptibility χ of the staggered polarization for PBCs [4]. Since there are no known analytical expressions for the asymptotic behaviour of P_0 for DWBCs we fall back on the leading corrections known for PBCs [45]. In the case of PBCs the leading correction for the peak position of χ is of the form $\ln^{-2} L$, and so for DWBCs one could make the educated guess that the

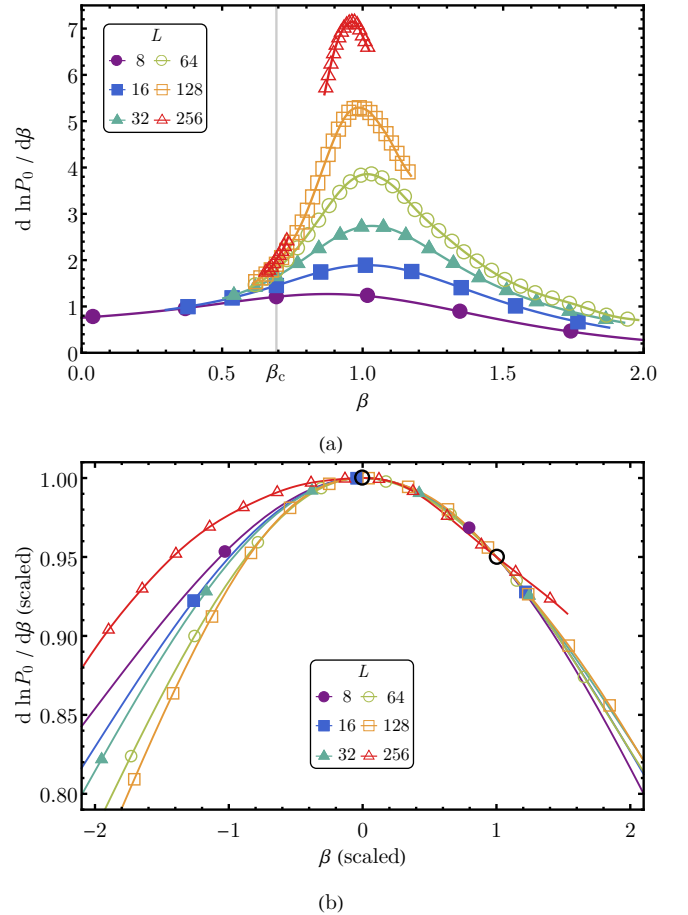


Figure 5. The observable $d \ln P_0 / d\beta$ is shown in (a) as a function of inverse temperature β for various system sizes up to $L = 256$. In the thermodynamic limit, under the assumption that P_0 is a valid order parameter, this function must have its peak at the critical point. In (b) the peak and the point where the curves attain 95% of their peak height (at higher β) are scaled on top of each other, with the two points indicated by black circles. From this collapse we extract the peak position and typical width for further analysis, cf. Fig. 6.

form of the peak of $d \ln P_0/d\beta$ scales like

$$x = A_x + B_x \ln^{-2} L + C_x \ln^{-3/2} L + D_x \ln^{-4} L, \quad (17)$$

where x is either the inverse peak height h_{\max}^{-1} , the peak width w , or the position β_{\max} of the peak. Fig. 6 shows these quantities as a function of $\ln^{-2} L$ with the best fit of Eq. (17) to the three characteristics. The best estimates from an unweighed fit to all data points for the peak height are $A_{h_{\max}^{-1}} = -0.01 \pm 0.03$, $B_{h_{\max}^{-1}} = 5.4 \pm 1.1$, $C_{h_{\max}^{-1}} = -3 \pm 3$, and $D_{h_{\max}^{-1}} = -2 \pm 3$. For the peak width the best estimates are given by $A_w = -0.009 \pm 0.009$, $B_w = 2.4 \pm 0.4$, $C_w = -5 \pm 1$, and $D_w = 3.0 \pm 0.8$. A similar fit for β_{\max} does not seem to work. Indeed, the best estimate for $A_{\beta_{\max}} = 0.83 \pm 0.02$ is far from the analytically known value $\beta_c = \ln 2$. Alternatively one could fix $A_{\beta_{\max}} = \beta_c$, in which case the fit does not go through the data in a clean fashion. Although this method does not reliably give an estimate for the critical point it does show the convergence of $d \ln P_0/d\beta$ to a Dirac delta-like distribution as the system size tends to infinity. From Fig. 6 we see that in practice direct computation using (13) cannot be used outside of the regime in which subleading finite-size corrections are important. Simulations reveal the decrease in β_{\max} for increasing system size.

C. Arctic curves

So far we have investigated global quantities. For inhomogeneous (not translationally invariant) systems such as the F -model with DWBCs such properties provide rather coarse information, as a lot of the local information is averaged away.

Fig. 7 shows the thermally averaged c -vertex density $\rho(c)$, together with several contour lines, for a system of linear size $L = 512$ at various temperatures: zero temperature ($\beta \rightarrow \infty$, $\Delta \rightarrow -\infty$), below the critical point ($\beta = 2\beta_c$, $\Delta = -7$), at the critical point ($\beta_c = \ln 2$, $\Delta = -1$), at the free-fermion point ($\beta = \beta_c/2$, $\Delta = 0$), and at infinite temperature ($\beta = 0$, $\Delta = 1/2$). For nonzero temperature 10 independent simulations, each yielding 10^6 measurements, were performed per temperature to calculate the local vertex density. We use horizontal, vertical, and diagonal reflection symmetry of $\rho(c)$ at a given Δ to get a smoother profile by averaging. At the centre $\rho(c)$ is always at a maximum. For zero temperature, the critical temperature, and the free-fermion point the maximal values are 1 and about $2/3$ and $1/2$, respectively. At low temperatures there is a AF region, with constant $\rho(c)$ close to unity signalling its ordered nature. As the temperature rises from zero a temperate region emerges that encloses the central AF region, completely engulfing it at the critical point, cf. [23]. The arctic cures, exactly known for $\Delta = -\infty$ and $\Delta = 0$ [26] and conjectured for $\Delta < 1$ [27–29] are also shown in Fig. 7. The outer contours are drawn at temperature-dependent values for $\rho(c)$ (see Table I) chosen such that

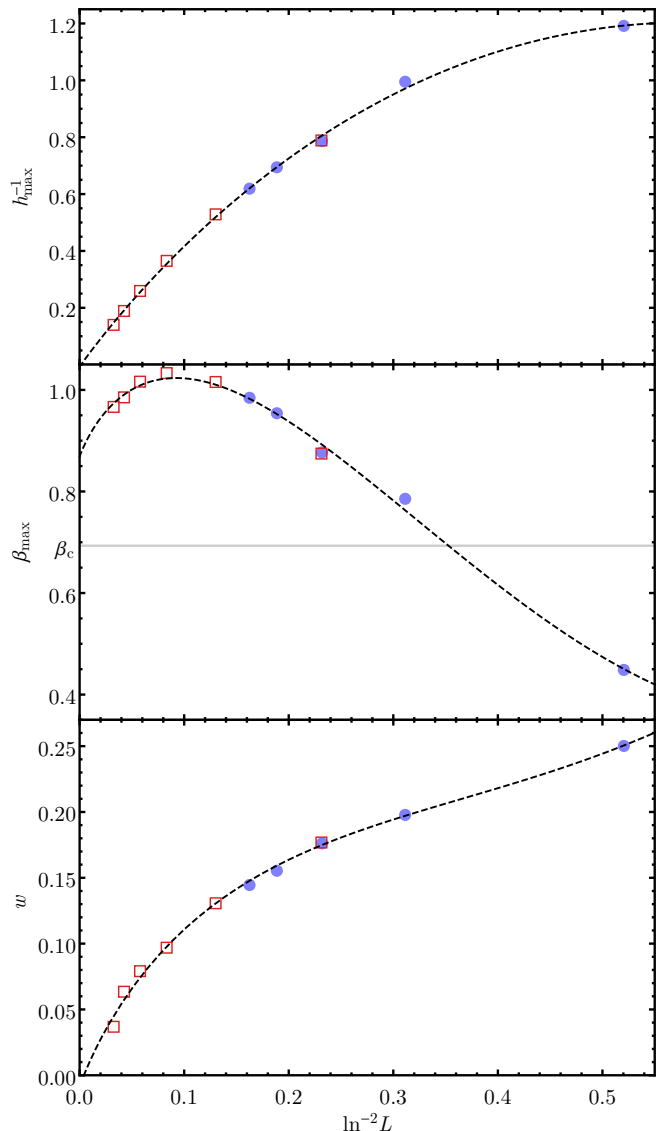


Figure 6. Values of the inverse peak height h_{\max}^{-1} (upper panel), peak position β_{\max} (central panel), and peak width w (lower panel) are shown for $d \ln P_0/d\beta$ up to system size $L = 256$ as a scaled function of $\ln^{-2} L$. Exact values for small system sizes obtained from Eq. (13) are shown as solid blue disks and best estimates obtained from our simulations as open red squares. The best unweighed fits of the form (17) are drawn as black dashed lines. For β_{\max} a fit through all data points results in a best estimate for the critical point $A_{\beta_{\max}} = 0.87 \pm 0.03$ far from the analytically known value $\beta_c = \ln 2 \approx 0.69$. For h_{\max}^{-1} ($A_{h_{\max}^{-1}} = -0.01 \pm 0.03$, $B_{h_{\max}^{-1}} = 5.4 \pm 1.1$, $C_{h_{\max}^{-1}} = -3 \pm 3$, $D_{h_{\max}^{-1}} = -2 \pm 3$) and w ($A_w = -0.009 \pm 0.009$, $B_w = 2.4 \pm 0.4$, $C_w = -5 \pm 1$, $D_w = 3.0 \pm 0.8$) the fits work well and are in agreement with $d \ln P_0/d\beta$ becoming a Dirac delta-like distribution as $L \rightarrow \infty$.

those contours are qualitatively comparable to the known and conjectured forms of the arctic curves. We see that our data match very well with the analytic expressions;

	(a)	(b)	(c)	(d)	(e)
β	∞	$2\beta_c$	$\beta_c = \ln 2$	$\beta_c/2$	0
Δ	$-\infty$	-7	-1	0	1/2
$\rho(c)$	0.500	0.012	0.021	0.018	0.014

Table I. The values for β and Δ at which the simulations for Fig. 7 (a)–(e) were performed are given together with the values for $\rho(c)$ at which the outer contours are drawn. For finite Δ this gives a measure of the deviation from the asymptotic values $\rho(c) = 0$ due to finite-size effects.

for nonzero temperature the deviation from zero of the values given in Table I is a measure of the influence of finite-size effects.

D. Oscillations in vertex densities

Finally we turn to the structure inside the temperate region. In Fig. 8 we show the thermally averaged densities ρ along the diagonal from the FE region dominated by b_- -vertices ($r = L/\sqrt{2}$, bottom left corner in Fig. 7) to the centre ($r = 0$) of a system of size $L = 512$ at the critical point $\Delta = -1$. Along this diagonal one has $\rho(a_+) = \rho(a_-)$. Moreover if one considers r to cover the full diagonal, $-L/\sqrt{2} \leq r \leq L/\sqrt{2}$, then $\rho(a_{\pm})$ and $\rho(c_{\pm})$ are even as functions of r while $r \mapsto -r$ reverses $\rho(b_+) \leftrightarrow \rho(b_-)$. This allows us — like we did for $\rho(c) = \rho(c_-) + \rho(c_+)$ in Fig. 7 — in Fig. 8 to use horizontal, vertical, and diagonal reflection to average for the densities of $\rho(a_{\pm})$ and $\rho(b_{\pm})$. Note that these transformations exchange $a_{\pm} \leftrightarrow b_{\pm}$, provided all arrows are reversed for diagonal reflection as required to preserve the boundary conditions.

Recently Lyberg et al. [24] numerically studied the arrow polarization density, whose asymptotic expression is known at $\Delta = 0$ [46]. The authors observed oscillations in the density for $\Delta < -1$. In Fig. 8 we observe oscillations for all of the vertex densities in the temperate region. The wavelengths of these oscillations are comparable functions of r for each of the vertices. For lower temperatures these oscillations are more pronounced yet the region in which they appear, viz. the temperate region, becomes smaller. The thermally averaged densities $\rho(c_+)$ and $\rho(c_-)$ are in antiphase (cf. Fig. 8) so these oscillations are masked if just $\rho(c)$ is considered as in Fig. 7. The complicated oscillatory behaviour in the temperate region can more clearly be seen from the thermally averaged c -vertex density difference $\delta\rho(c) := \rho(c_-) - \rho(c_+)$. To study the dependence on the system size of the oscillations in the temperate region Fig. 9 shows $\delta\rho(c)$ along the diagonal for system sizes $L = 32$ up to $L = 512$. The wavelength of the oscillations is always largest at the edges of the temperate region. We observe a sublinear growth of the wavelength in L . A best unweighed fit to the distance between the centre of the system ($r = 0$) and the position of the maximum of $\delta\rho(c)$ gives

$(0.67 \pm 0.06)L^{(0.553 \pm 0.016)}$. Such a fit cannot be made for the maximal amplitude as our data is not accurate enough to distinguish between logarithmic or power-law behaviour. Still Fig. 9 does clearly show that the average wave amplitude monotonically decreases with system size, suggesting that the oscillations are finite-size effects.

Fig. 10 shows the profile of $\delta\rho(c)$ for systems at $\Delta = -1$ and $\Delta = -7$. Inside the temperate region there are at least two types of oscillations: one type, let us call them ‘AF oscillations’, follows the boundary between the AF-frozen and temperate regions (which for $\Delta \rightarrow -1$ degenerates to the horizontal and vertical lines separating the quadrants), while the other type, ‘FE oscillations’, follows the contours of the arctic curve between the temperate and FE-frozen regions. (These types of oscillations may be discerned in [24, Fig. 6] too.)

Interestingly, upon closer inspection of Fig. 10 we observe a checkerboard-like pattern inside the AF oscillations (cf. [24, Fig. 6, $\Delta = -10$]), signalling site-to-site anti-correlations for $\rho(c_{\pm})$ that persist over long distances along the oscillations, and justifying the name ‘AF’ for these types of oscillations. The checkerboards in adjacent oscillations are opposite: these oscillations are separated by an even number of vertices along every row and every column. Note that such checkerboard-like anti-correlations are invisible when one focusses on the densities along the diagonal. Next we turn to the FE oscillations near the frozen region dominated by b_- . The profile of $\delta\rho(b)$ reveals that the interior of these oscillations are again dominated by b_- . (We have chosen not to include this profile in the present work as it essentially just shows the b_- -oscillations that can be seen in Fig. 8. From the profile of $\delta\rho(a)$, cf. the green/red plots in [24, Fig. 6], it can be seen that near the top-left and bottom-right corners in Fig. 10 the role of b_- gradually start being taken by the a_{\pm} -vertices that are favoured in the FE-frozen regions of the corresponding neighbouring quadrants.) Using symmetry arguments similar statements are true for the other quadrants. Fig. 10 further shows that the regions between the FE oscillations are dominated by c_- -vertices ($\delta\rho(c) > 0$) to account for the constraint $\#c_- > \#c_+$ imposed by the DWBCs.

To justify our observations let us explain in more detail how Fig. 10 was obtained. We use the same data as for Fig. 7, based on 10 independent simulations each with 10^6 measurements of local vertex density. Recall from Sec. III that there are (reference) configurations corresponding to maximal and minimal height profiles. The graph of the phase space of the six-vertex model with DWBCs consists of two components, one containing the highest profile and the other the lowest profile, which are connected by a thin neck [23] containing the AF ground state(s) amongst others. Since we always start from the low reference configuration, our simulations typically produce states in the same part of the phase space, containing the lower configurations. In particular, for L even and low temperatures we tend to end up with the slightly lower of the two ground states. In the

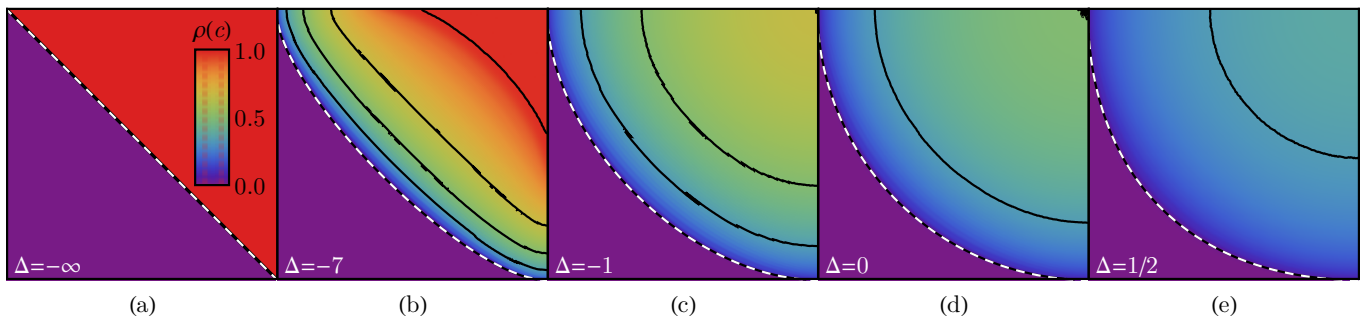


Figure 7. The thermally averaged density $\rho(c)$ of c -vertices at $L = 512$ show phase separation at different temperatures. The density lies between zero (shown in purple) and one (red). At zero temperature the AF region is a diamond (a). At slightly elevated temperatures (b) the AF and FE regions are separated by a temperate region. As the temperature increases past its critical value (c), at which the AF region disappears, the arctic curve deforms to a circle at the free-fermion point (d). The system at infinite temperature is shown in (e), in which the arctic curve is a rectangle with (very) rounded corners. The black solid contours are drawn at $\rho(c) = 1/3, 1/2, 2/3$, and 0.98, as well as at temperature-dependent values (see Table I) to match the known arctic curves [26–29] shown as white dashed lines.

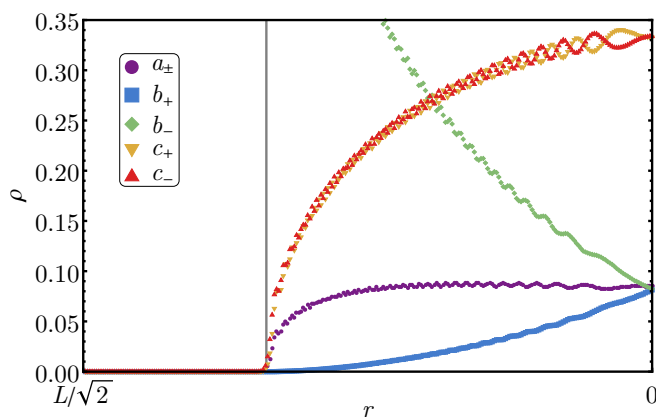


Figure 8. The thermally averaged densities ρ for all six vertices in a system of linear size $L = 512$ at the critical point $\Delta = -1$ are shown along the diagonal from the b_- -dominated FE region to the centre at $r = 0$. The grey vertical line marks the transition between the FE and temperate region [29]. Each vertex density oscillates in the temperate region. Note that $\rho(c_{\pm})$ are in antiphase around their average.

FE-frozen region there are no c vertices and so $\delta\rho(c) = 0$ for any configuration. For any single configuration the AF-frozen region, present below the critical temperature, is characterized by a high anti-correlation for $\delta\rho(c)$ at neighbouring sites. However, when L is even for every slightly lower configuration there is a slightly higher one with the same energy, so after averaging $\delta\rho(c)$ vanishes in the AF region too in that case. We use the above reflection symmetries to produce further (slightly higher) configurations from those obtained from our simulations; averaging over these configurations we obtain the profile for $\delta\rho(c)$ shown in Fig. 10, which indeed vanishes both in the FE and AF regions. For even as well as odd L the site-to-site anti-correlations between the AF oscillations in the temperate region survive this averaging.

Besides the AF and FE oscillations following the curves

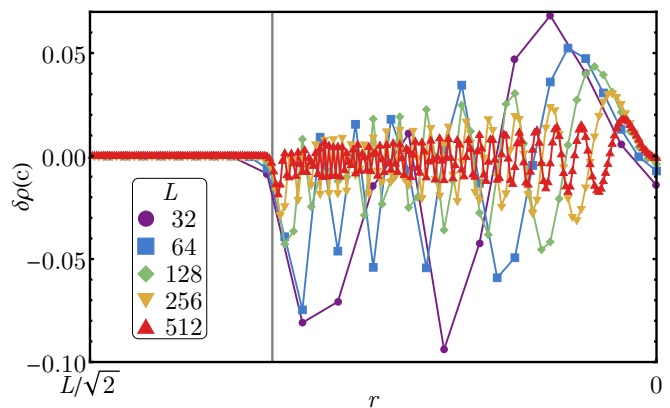


Figure 9. The difference $\delta\rho(c)$ is shown as a function of distance r along the diagonal to the centre (at $r = 0$) for systems up to size $L = 512$. The coloured lines are a guide to the eye and the grey vertical line denotes the transition between the FE-frozen and temperate region as in [29]. The wavelength of the oscillations seems to increase sublinearly while the average wave amplitude decreases monotonically with system size, suggesting that this are finite-size effects.

separating the temperate and corresponding frozen regions there are also additional ‘higher’ oscillations in $\delta\rho(c)$ that form intricate patterns in the temperate region that are barely visible in Fig. 10. To visualize these oscillations more clearly in Fig. 11 we truncate $\delta\rho(c)$ at 10% of the minimal and maximal values from the upper panel of Fig. 10. These higher oscillations exhibit several ‘saddle-point’-like patterns around the centre of the temperate region.

V. SUMMARY AND OUTLOOK

In this work we have used Monte Carlo simulations to study the F -model with DWBCs. Although a closed

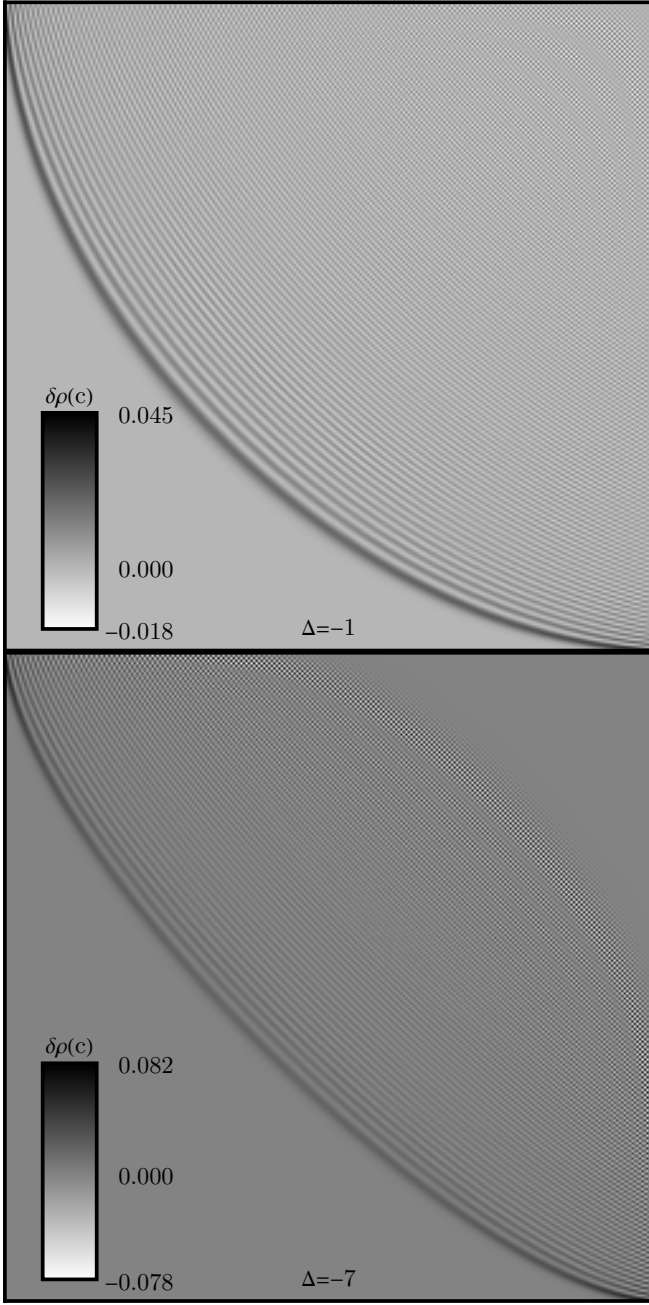


Figure 10. [High quality online.] The thermally averaged density difference $\delta\rho(c)$ is shown for a system of size $L = 512$ at $\Delta = -1$ (upper panel) and $\Delta = -7$ (lower panel). The FE-frozen region in the bottom left contains only b_- -vertices. Below the critical point the AF-frozen region appears (lower panel) in which $\delta\rho(c) = 0$ due to the two-fold degeneracy for even L . Inside the intermediate temperate region at least two types of oscillations are visible. There appear to be checkerboard-like patterns in the ‘AF oscillations’ even after thermal averaging, with opposite checkerboards in neighbouring oscillations. The ‘FE oscillations’ are dominated by the vertices constituting the FE-frozen region (here b_-), with $\delta\rho(c) > 0$ between them.

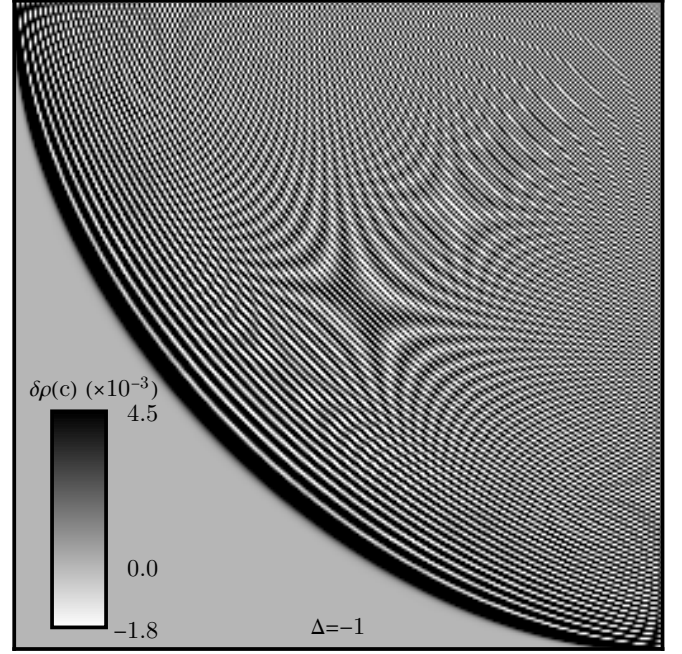


Figure 11. [High quality online.] The thermally averaged c_{\pm} -density difference $\delta\rho(c)$ for size $L = 512$ at $\Delta = -1$, truncated at 10% of the values from the upper panel of Fig. 10. This reveals very weak (notice the scale!) ‘higher’ oscillations in the temperate region with various ‘saddle-point’-like features; we can distinguish at least four of these along the diagonal, and more along the top and right.

form for the partition function is analytically known for all system sizes in practice it is particularly useful for the exact computation of certain observables for fairly small systems and to obtain the asymptotic form and its finite-size corrections. Simulations allow for the investigation of systems of moderate size to complement such analytic results as well as to study properties that are not (yet) understood from an analytic point of view.

We have given best estimates for the parameters in the first three subleading finite-size corrections to the energy derived from the asymptotic partition function in Eq. (5) at the critical point by fits to the average energies obtained from simulations. This tests the reliability of our simulations; they are precise enough to distinguish the different subleading corrections (Fig. 4). The best estimates for the parameters suggest that the first subleading correction is non-negligible in comparison to the leading correction even for macroscopically sized systems, with $L \sim 10^{21}$. We find $\alpha = 1.91 \pm 0.39$ for a previously unknown parameter in the asymptotic expression (5) of the domain-wall partition function in the disordered regime found by Bleher and Fokin [18].

Following joint work with Duine and Barkema [4] we have further investigated the order parameter based on the staggered polarization P_0 , of which we gave a description in the framework of the quantum-inverse scattering method (QISM). From a theoretical point of view

it would be interesting to explore whether it is possible to adapt Baxter’s work [30] to obtain an exact expression for P_0 in the case of domain walls, at least in the thermodynamic limit, but we have not done so in the present work. If P_0 is a true order parameter for the model’s IOPT, i.e. it is constant on one side of the critical temperature and smoothly starts to change at the phase transition, then the observable $d \ln P_0 / d\beta$ must by definition have a divergence at the critical point for infinitely large systems. Using finite-size scaling, and extrapolating to the asymptotic case we have found that $d \ln P_0 / d\beta$ does indeed converge to a delta-distribution, see Fig. 6, although it fails to give an accurate estimate for the (analytically known) temperature at which the phase transition occurs. Of course the DWBCs together with the ice rule make the system that we have investigated rather special; the observable proposed in [4] may still be useful for the investigation of other models exhibiting an IOPT. One could also try using the susceptibility of P_0 instead; most of its peaks lie outside our simulation range, though the peaks that are visible appear to have a comparable quality for finite-size scaling.

In addition to these global (spatially averaged) properties we have studied local properties of the system. The profiles of the c -vertex density $\rho(c)$ obtained for systems of size $L = 512$ at various temperatures with $\Delta \leq 1/2$ are shown in Fig. 7. In the antiferroelectric phase (AF) our simulations corroborate the coexistence of three spatially separated phases as found in [22, 23], with a flat central region exhibiting frozen AF order surrounded by a disordered ‘temperate’ region and ferroelectrically ordered corners. Our data agree very well with the arctic curves conjectured by Colomo and Pronko [28] and Colomo, Pronko and Zinn-Justin [29]. It would be desirable to have similar analytic expressions for the limit shape sep-

arating the temperate and AF-frozen regions.

Regarding the structure inside the temperate region our simulations confirm the oscillations recently found by Lyberg et al. [24], see Fig. 8. Our data suggest that the oscillations are finite-size effects: their wavelengths appear to grow sublinearly and their average amplitudes decrease with system size (Fig. 9). Our most detailed result regarding the structure of the temperate region are Figs. 10 and 11. We find several types of oscillations. The ‘AF oscillations’ close to the AF-frozen region appear to be made up of chequerboards of c_{\pm} -vertices that (unlike the AF region in case of even L) survive thermal averaging for even as well as odd L , and are opposite between neighbouring oscillations. The ‘FE oscillations’ near the FE-frozen region are dominated by the vertices constituting that frozen region; in between these oscillations there is a surplus of the type of c -vertices favoured by the DWBCs. In addition there appear to be weak ‘higher oscillations’ in c_{\pm} -densities, forming various ‘saddle-point’-like patterns. A more quantitative understanding of these vertex-density oscillations in the temperate region would be very interesting.

VI. ACKNOWLEDGEMENTS

We thank P. Zinn-Justin for bringing CFTP under our attention, and G. Barkema for feedback on an earlier version of this work. The authors also thank the Institute for Theoretical Physics at Utrecht University for the hospitality during the course of this work. JL gratefully acknowledges support from the Knut and Alice Wallenberg Foundation (KAW). This work is part of the D-ITP consortium, a program of the Netherlands Organisation for Scientific Research (NWO) that is funded by the Dutch Ministry of Education, Culture and Science (OCW).

-
- [1] Corresponding author.
 - [2] F. Rys, *Helv. Phys. Acta* **36**, 537 (1963).
 - [3] E. H. Lieb, *Phys. Rev. Lett.* **18**, 1046 (1967).
 - [4] R. Keesman, J. Lamers, R. A. Duine, and G. T. Barkema, *J. Stat. Mech.: Theor. Exp.* **2016**, 093201 (2016), arXiv:1605.08876 [cond-mat.stat-mech].
 - [5] To see that the ice rule is crucial here consider the eight-vertex model, where the ice rule is slightly relaxed. This model cannot be tackled with a straightforward Bethe-ansatz analysis, and its thermodynamics are insensitive to the choice of boundary conditions, cf. [10] below.
 - [6] J. Lamers, *PoS Modave2014*, 001 (2014), arXiv:1501.06805 [math-ph].
 - [7] V. Korepin and P. Zinn-Justin, *J. Phys. A: Math. Gen.* **33**, 7053 (2000), arXiv:cond-mat/0004250.
 - [8] P. Zinn-Justin, “The influence of boundary conditions in the six-vertex model,” (2002), arXiv:cond-mat/0205192.
 - [9] S. K. Jain, V. Juričić, and G. T. Barkema, *Phys. Rev. B* **94**, 020102 (2016), arXiv:1607.03638 [cond-mat.mtrl-sci].
 - [10] H. J. Brascamp, H. Kunz, and F. Y. Wu, *J. Math. Phys.* **14**, 1927 (1973).
 - [11] T. S. Tavares, G. A. P. Ribeiro, and V. E. Korepin, *J. Phys. A: Math. Theor.* **48**, 454004 (2015), arXiv:1509.06324 [cond-mat.stat-mech].
 - [12] V. E. Korepin, *Commun. Math. Phys.* **86**, 391 (1982).
 - [13] W. H. Mills, D. P. Robbins, and H. Rumsey, *J. Combin. Theory Ser. A* **34**, 340 (1983).
 - [14] G. Kuperberg, *Inter. Math. Res. Notes* **1996**, 139 (1996), arXiv:math/9712207 [math.CO].
 - [15] D. Bressoud, *Proofs and confirmations: the story of the alternating sign matrix conjecture* (Cambridge University Press, 1999).
 - [16] I. Kostov, *J. Phys. A: Math. Theor.* **45**, 494018 (2012), arXiv:1205.4412 [hep-th]; Y. Jiang, S. Komatsu, I. Kostov, and D. Serban, *J. Phys. A: Math. Theor.* **49**, 454003 (2016), arXiv:1604.03575 [hep-th]; A. G. Izergin, D. A. Coker, and V. E. Korepin, *J. Phys. A: Math. Gen.* **25**, 4315 (1992).
 - [17] P. Zinn-Justin, *Phys. Rev. E* **62**, 3411 (2000), arXiv:math-ph/0005008.
 - [18] P. Bleher and V. Fokin, *Commun. Math. Phys.* **268**, 223 (2006), arXiv:math-ph/0510033.

- [19] P. Bleher and K. Liechty, Commun. Math. Phys. **286**, 777 (2009), arXiv:0904.3088 [math-ph].
- [20] P. Bleher and T. Bothner, Random Matrices: Theory Appl. **01**, 1250012 (2012), arXiv:1208.6276 [math-ph].
- [21] R. J. Baxter, *Exactly solved models in statistical mechanics* (Dover Publications, 2007).
- [22] O. F. Syljuåsen and M. B. Zvonarev, Phys. Rev. E **70**, 016118 (2004), arXiv:cond-mat/0401491.
- [23] D. Allison and N. Reshetikhin, Ann. Inst. Fourier (Grenoble) **55**, 1847 (2005), arXiv:cond-mat/0502314.
- [24] I. Lyberg, V. Korepin, and J. Viti, “The density profile of the six vertex model with domain wall boundary conditions,” (2016), arXiv:1612.06758 [cond-mat.stat-mech].
- [25] W. Jockusch, J. Propp, and P. Shor, “Random domino tilings and the arctic circle theorem,” (1998), arXiv:math/9801068 [math.CO].
- [26] K. Johansson, Ann. Prob. **33**, 1 (2005), arXiv:math/0306216 [math.PR]; P. L. Ferrari and H. Spohn, J. Phys. A: Math. Gen. **39**, 10297 (2006), arXiv:cond-mat/0605406 [cond-mat.stat-mech].
- [27] F. Colomo and A. G. Pronko, SIAM J. Discrete Math. **24**, 1558 (2010), arXiv:0803.2697 [math-ph].
- [28] F. Colomo and A. G. Pronko, J. Stat. Phys. **138**, 662 (2010), arXiv:0907.1264 [math-ph].
- [29] F. Colomo, A. G. Pronko, and P. Zinn-Justin, J. Stat. Mech.: Theor. Exp. **2010**, L03002 (2010), arXiv:1001.2189 [math-ph].
- [30] R. J. Baxter, J. Stat. Phys. **9**, 145 (1973).
- [31] E. H. Lieb, Phys. Rev. Lett. **19**, 108 (1967).
- [32] P. Bleher and K. Liechty, J. Stat. Phys. **134**, 463 (2009), arXiv:0802.0690 [math-ph].
- [33] K. Eloranta, J. Stat. Phys. **96**, 1091 (1999).
- [34] A. G. Izergin, Sov. Phys. Dokl. **32**, 878 (1987).
- [35] G. Kuperberg, Ann. of Math. **156**, 835 (2002), arXiv:math/0008184 [math.CO].
- [36] Note that $R(s) = (I \otimes \delta_{-s}) R(0) (I \otimes \delta_s)$ for I the 2×2 identity matrix, $\delta_s := \exp(s\sigma^z/2)$ with σ^z the third Pauli matrix, and $R(0)$ the R -matrix of the ordinary (zero-field) six-vertex model. Direct horizontal and vertical fields would correspond to $(\delta_h \otimes \delta_v) R(0) (\delta_h \otimes \delta_v)$, which can be used to compute the direct polarization in a similar fashion.
- [37] The partition function for an $L \times L$ lattice with L even and PBCs is obtained by defining the staggered transfer matrix $t(s) := \text{tr} T(s) = A(s) + D(s)$, where $A(s)$ and $D(s)$ are similar to (12) but with both arrows pointing left and right, respectively. Then the partition function is $Z_L^{\text{per}}(s) = \text{tr} \{ [t(-s) t(s)]^{L/2} \}$.
- [38] H. v. Beijeren, Phys. Rev. Lett. **38**, 993 (1977).
- [39] J. G. Propp and D. B. Wilson, Random Struct. Algor. **9**, 223 (1996); J. Propp and D. Wilson, in *Microsurveys in discrete probability*, Discrete Math. Theoret. Comput. Sci., Vol. 41, edited by D. Aldous and J. Propp (AMS, 1998) pp. 181–192.
- [40] J.-S. Wang, R. H. Swendsen, and R. Kotecký, Phys. Rev. B **42**, 2465 (1990).
- [41] G. T. Barkema and M. E. J. Newman, Phys. Rev. E **57**, 1155 (1998).
- [42] E. Marinari and G. Parisi, Europhys. Lett. **19**, 6 (1992).
- [43] J. P. Valleau and D. N. Card, The Journal of Chemical Physics **57**, 5457 (1972).
- [44] A. M. Ferrenberg and R. H. Swendsen, Phys. Rev. Lett. **63**, 1195 (1989).
- [45] M. Weigel and W. Janke, J. Phys. A **38**, 7067 (2005), arXiv:cond-mat/0501222.
- [46] N. Allegra, J. Dubail, J.-M. Stéphan, and J. Viti, J. Stat. Mech.: Theor. Exp. **5**, 053108 (2016), arXiv:1512.02872 [cond-mat.stat-mech].